PHYSICAL REVIEW FLUIDS **9**, 083102 (2024)

Vortex dynamics in healthy and pro-atherogenic carotid artery bifurcation models

Nora Caroline Wild,[1] Kartik V. Bulusu,[1] and Michael W. Plesniak[2,*]
[1] *Department of Mechanical and Aerospace Engineering,*
The George Washington University, 800 22nd Street NW, Washington, DC 20052, USA
[2] *Department of Mechanical and Aerospace Engineering and Department of Biomedical Engineering,*
The George Washington University, 800 22nd Street NW, Washington, DC 20052, USA

(Received 8 March 2024; accepted 24 July 2024; published 27 August 2024)

Carotid artery atherosclerosis is a significant contributor to mortality in the United States. While it is recognized that low wall-shear stresses trigger plaque formation, there is a limited comprehension of the internal vortical structures that impact these stresses and how they differ between a healthy and a disease-prone, high-risk patient cohort. Our objective is to determine which driving factors, such as anatomical features (artery geometry) and mass-flow split, govern vortex behavior. Physiological pulsatile flow computational fluid dynamics simulations were performed on a "healthy" and a "disease-prone" carotid artery bifurcation model. Geometry and flow effects are investigated separately by simulating a third hybrid model having a healthy geometry with outlet boundary conditions imposing disease-prone flow conditions. This "unhealthy ΔP" model recreated disease-prone mass-flow split and internal carotid artery sinus axial pressure gradient conditions in a healthy carotid artery bifurcation geometry. The results of our study revealed that the main vortex's time of formation is primarily dictated by carotid artery bifurcation geometry, whereas its lifespan is determined by the flow conditions. The main vortex's spatial expansion, as well as its circulation decay rate, are dictated by the geometry, not the flow conditions. We conclude that a high internal carotid artery mass flow rate and a higher favorable pressure gradient maximum magnitude occurring near peak systole are strong indicators of a high predisposition towards atherogenesis.

DOI: 10.1103/PhysRevFluids.9.083102

I. INTRODUCTION

In the United States, approximately half of all fatalities result from cardiovascular diseases, including strokes and heart attacks [1]. Strokes alone impact more than 15 million individuals annually [2], with up to 30% of these cases attributed to carotid artery disease [2,3]. Carotid artery disease typically manifests at the carotid artery bifurcation (CAB) located in the neck. The common carotid artery (CCA) diverges from the aorta, subsequently branching into the internal (ICA) and external (ECA) carotid arteries, with CAB representing the point where CCA divides into ICA and ECA. The ICA and ECA serve as conduits for blood transport to the brain and face, respectively [1]. Atherosclerotic plaques are among the most characteristic carotid artery diseases. The growth or rupture of these plaques can impede blood supply to the downstream brain vasculature. Atherosclerosis, defined as the localized accumulation of cholesterol and lipids on the arterial wall, predominantly occurs in regions of intricate vessel geometry, such as bifurcations, and primarily affects large- and medium-sized blood vessels [1–6]. The innermost layer within

---

[*] Contact author: plesniak@gwu.edu

the vessel lumen, known as the endothelium, experiences wall-shear stresses present throughout the entire cardiovascular system [2,3]. These shear stresses, induced by blood flow across the vessel lumen, are essential for maintaining the health of endothelial cells [7]. Atherosclerosis develops when there is a presence of pathological flow and, consequently, abnormal shear stresses, characterized by variations in magnitude or significant temporal fluctuations [1,8]. Endothelial cells sense and transmit these pathological mechanical forces, leading to cellular dysfunction through a mechanotransduction process [9,10]. In atherosclerotic regions, the flow becomes disrupted, resulting in lower shear stress than normal [1,11], and substantially varying spatial shear stress gradients [12–15]. Given their pivotal role in the initiation of cardiovascular diseases, shear stresses that trigger plaque formation at the carotid artery bifurcation are of considerable clinical interest and are under investigation using computational fluid dynamic (CFD) simulations. Computational fluid dynamics (CFD) investigations involving patient-specific artery geometries [16] and simplified artery models are frequently documented in the literature [17–20]. The utilization of simplified patient-averaged models contributes to a broader comprehension of general flow phenomena in the carotid artery bifurcation and their role in atherosclerosis. Typically, these models portray "healthy" vessel geometries [21] based on general patient averages, without emphasizing the actual risk for future plaque development within patient cohorts. Atherosclerotic vessel geometries are commonly simulated under diseased conditions [16,22], introducing a local narrowing of the vessel diameter in the form of plaque buildup (stenosis). Flow separation in the ICA sinus correlates with higher atherosclerosis risk [1,17–20,23–25]. Additionally, sinus geometry, especially a larger bifurcation angle and asymmetry, is indicative of increased risk [26,27]. This paper introduces an approach by highlighting a patient-cohort predisposition toward plaque formation, modeling a nondiseased but disease-prone carotid artery bifurcation (CAB). To the best of our knowledge, there is no published study investigating flow fields and vortical structures, along with their influence on wall-shear-stress distribution, in carotid artery bifurcation geometries with a distinct predisposition towards the formation of atherosclerotic plaques. Vortices, influencing the distribution of wall-shear stress [28–30], play a crucial role in understanding the onset of cardiovascular diseases [31]. However, only a few studies delve into the exploration of vortices [16]. Notably, Gijsen *et al.* observed the development of Dean vortices postbifurcation under steady flow conditions. This phenomenon arises from the curvature transitioning from CCA to ICA, leading to the transport of fluid towards the nondivider ICA wall and inducing flow reversal [23]. Previous studies often limit their analysis to two-dimensional secondary flows. In contrast, Chen *et al.* (2020) delved into three-dimensional vortical structures within the carotid artery bifurcation. Their findings revealed variations in secondary flows based on different bifurcation geometries. Specifically, a larger ICA bifurcation angle resulted in stronger secondary flows during inflow acceleration, with Dean vortices forming at an ICA bifurcation angle around 30 °C [32].

State-of-the-art clinical imaging methods, such as ultrasonography [33] or 4D flow MRI [34,35], offer precise visualization of carotid artery bifurcation (CAB) flow in patients. Emerging techniques like vector flow imaging provide intuitive and quantitative imaging of vortical structures [36]. Medical imaging advancements enable the identification of vortical structures, by extracting vortical structures using the λ_2 criterion [35] and determining vortex core positions, like vortex rings in the heart [34], making it accessible for clinicians [37]. Changes in the development of a main vortex are linked to pathological cardiovascular flow and function, such as diastolic vortex formation in the left ventricle [34]. Despite these possibilities, the impact of three-dimensional vortices in the CAB on potentially pro-atherogenic shear stress distributions is not well understood, which limits the prospective potential for clinicians to use similar vortex analysis for risk assessment in the CAB. Our previous studies started to address this knowledge gap. We investigated flow, shear stress, and vortical structures in a "healthy" and "disease-prone" carotid artery bifurcation model. The disease-prone geometry experiences a more equal flow split between ICA and ECA, larger flow separation in the sinus, and lower time-averaged-wall-shear stresses spanning over a larger area than the healthy geometry [38]. For both geometries, a main hairpin vortical structure was found in the sinus, which was expected to play a physiological beneficial role as it locally increases wall-shear stresses. In the disease-prone geometry, this vortical structure had a significantly shorter lifespan, reducing its beneficial effect. The earlier deterioration of this hairpin vortical structure coincided with a much weaker axial favorable pressure gradient acting over the ICA sinus in the disease-prone geometry [39,40].

In this study, we consider a representative healthy vessel geometry, a pro-atherogenic disease-prone geometry, and a developed hypothetical model consisting of healthy geometry with flow conditions mimicking those in a disease-prone geometry. Our previous study increased the fundamental understanding of vortex evolution over the cardiac cycle, enabling the characterization of differences between healthy and pathological vortical structures. The uniqueness of this study is determining driving factors of shortened vortex lifespan causing atherosclerotic plaque-triggering shear stress conditions. This study aims to elucidate which underlying parameter—geometry and axial pressure gradient—is responsible for the differences in specific vortex behaviors. Hemodynamics in "healthy," "disease-prone," and "'unhealthy ΔP" CAB geometries are investigated using three-dimensional computational fluid dynamics (CFD) simulations with physiological pulsatile flow. This study further aims to evaluate the potential of vortex-based clinical evaluation to assess carotid bifurcation atherosclerosis risk. This study's objective is to identify the physical driving factors, such as geometry or pressure gradients along the artery, that determine a pathological vortex behavior. Identifying those physical driving factors increases fundamental understanding of the vortex dynamics in artery blood flow. Furthermore, this has potential future application in clinical decision making, as some of those potential driving factors, such as the single-value axial pressure gradient over the sinus, are accessible more easily through clinical methods than the full vortex dynamics. The results aim to correlate changes in flow split and axial pressure gradient over the ICA sinus to pro-atherogenic vortex behavior, aiming for prospective transfer into clinical atherosclerosis early-detection methods. Thus, identifying the vortex core in the present study is highly correlated to the biomedical context of disease onset and progression.

II. METHODS

Methods used in this paper will be discussed in the following section. First, the generation of three carotid artery bifurcation models is explained. Second, computational fluid dynamic methods, as well as the used boundary conditions are described. Third, implemented vortex identification methods are detailed.

A. Carotid artery bifurcation geometry

A healthy carotid artery bifurcation geometry [Fig. 1(a)] was modeled based on anatomical features of a healthy population [41–43]. This represents a circular 6.5 mm CCA inlet diameter, and the CCA diameter tapers continuously towards the symmetric bifurcation, which branches with an angle of 60° into the internal and external carotid artery. The model includes the internal carotid artery sinus, as it is the crucial region for plaque formation. To improve numerical convergence and prevent nonphysical reverse flow at the outlets, straight constant diameter entry and exit lengths were added at the inlet and outlets.

The arteries' geometry is one of the factors that influences increased atherosclerosis risk. There are two clinically identified main geometrical risk factors: (1) a larger bifurcation angle, especially larger ICA angles, and (2) a small ICA/CCA diameter ratio [44–46]. To investigate those risk factors, a disease-prone geometry is modeled, incorporating these risk factors [Fig. 1(b)]. This disease-prone model has an asymmetric branching angle due to an 15° increase of the internal carotid artery angle [44], and in addition the ICA/CCA diameter was reduced to 0.5 [45,47] by reducing ICA diameter downstream of the sinus. Geometric differences between the two geometries are tabulated in Table I. The comparison between a healthy and a disease-prone geometry allowed us to identify the differences in flow fields and formation of vortical structures and their influence on an pro-atherogenic wall-shear-stress distribution, in our previous studies [38,39].

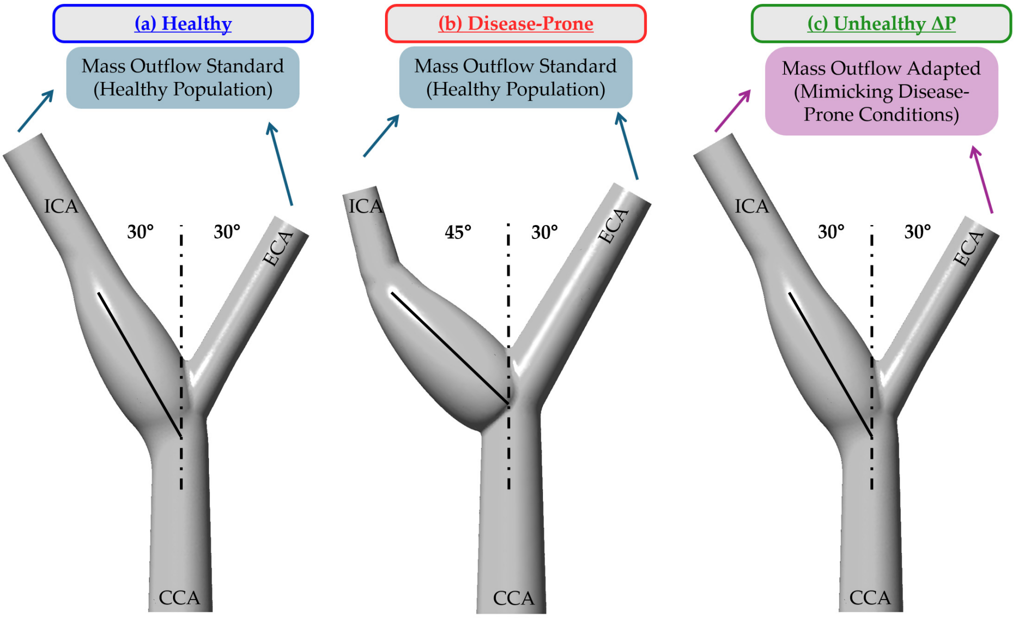

FIG. 1. Healthy (left), disease-prone (middle), and unhealthy ΔP (right) model geometry of the carotid artery bifurcation. (a) Symmetric total branching angle with 30° ICA branching angle, characteristic of a healthy geometry. (b) Asymmetric total branching angle with 45° ICA branching angle, characteristic of a disease-prone geometry. (c) Healthy geometrical features with adapted outlet boundary conditions to achieve mass flow split corresponding to disease-prone conditions.

1. Healthy model with disease-prone conditions

Our previous studies have revealed significant wall-shear-stress differences between the healthy and disease-prone geometry, where the disease-prone geometry experiences an atherogenic environment [38]. Another study showed the presence of a main hairpin vortical structure in the critical sinus region, which induces healthy levels of wall-shear stress locally. This vortical structure has a much shorter lifespan in the disease-prone geometry, shortening the timeframe for its positive impact. The presented study aims to investigate the underlying mechanisms and causes for the different behavior in vortical structure formation, lifespan and deterioration. The described geometry differences between the healthy and disease-prone models result in different flow resistances and thus influence the mass outflow and the axial pressure gradient acting throughout the geometry. The separate effects of the geometry and the pressure gradient are studied herein. Thus, an additional simulation is run based on the healthy geometry with altered pressure gradient. The outlet boundary conditions are manipulated to achieve mass flow outflows as well as sinus axial pressure gradients

TABLE I. Main anatomical risk factors in CAB. Showing geometrical differences between healthy and disease-prone model geometry. Diameter ratio: CCA diameter measured at inlet, ICA diameter measured downstream of sinus.

Geometrical risk factor	Healthy model	Disease-prone model
Total CAB branching angle	60°	75°
ICA branching angle	30°	45°
$\frac{D_{ICA}}{D_{CCA}}$	0.7	0.5

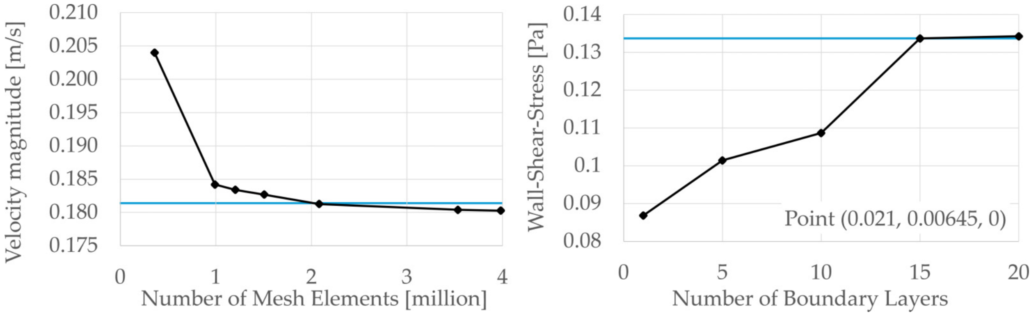

FIG. 2. Mesh independence study of core mesh and boundary layer mesh by tracking core velocity magnitude (left) and wall-shear stress (right) at a given point, respectively.

that replicate the conditions present in the disease-prone geometry. The model geometry is shown in Fig. 1(c); the description of the adapted outlet boundary conditions can be found in Sec. II B 2.

B. Computational fluid dynamics (CFD)

The transient flow in all three carotid artery bifurcation models was simulated using three-dimensional computational fluid dynamics (CFD). The models were created in ANSYS® Design-Modeler, the spatial meshing performed in the ANSYS® meshing tool. The physics flow solver used is ANSYS® FLUENT Academic Research Mechanical Release 2021 R1. Equations are solved using a finite volume method and a pressure-based solver under time-dependent laminar conditions on the George Washington University high-performance computing (HPC) cluster Pegasus. For results postprocessing ANSYS® FLUENT, Python JUPYTER Notebook 6.4.8, and MATLAB R2021a are used.

1. Spatial and time discretization

The ANSYS® meshing tool was used to create the volume and boundary layer mesh. High spatial resolution and accuracy is ensured by performing a mesh independence study on the bulk flow velocity and critical wall-shear stress (see Fig. 2). A tetrahedral meshing was chosen for the core region resulting in a final mesh of 2 080 502 elements. For details on the mesh independence study see [38]. For independence on the initial solution and a steady-state solution, the third physiological cycle is extracted for result analysis. Results are analyzed within or averaged over one single cardiac cycle, which is in agreement with published literature, as flow variations between cycles in small vessels, such as the ICA, are found to be minimal [48]. To achieve low computational cost a time step of 0.000625 s is chosen, ensuring the maximum Courant-Friedrichs-Lewy (CFL) number remains smaller than 1 to all times of the flow cycle.

2. Boundary conditions

Boundary conditions are set at the rigid wall as a no-slip condition and as transient conditions at the inlet and both outlets. Ku *et al.* [26] reported previously that the effect of wall compliance is significantly smaller than that of the geometry, specifically bifurcation angle, or flow conditions, such as inflow pulse waveform or flow partition ratio. This study, among others, informed the validity of a rigid wall approximation. A velocity inlet boundary condition is chosen at the CCA following the time-dependent spatially uniform inflow waveform given in Fig. 3. The inflow velocity peaks at a corresponding Reynolds number (Re) of 1530 and has an average Re of 385. The velocity is defined as Reynolds number multiplied by kinematic viscosity and divided by CCA diameter. At the CCA, the velocity inlet is provided with a spatially uniform, time-dependent waveform function. The physiological-pulsatile inflow velocity waveform is patient-averaged data based on

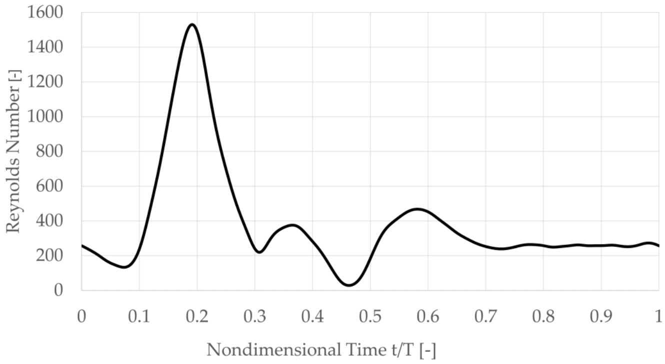

FIG. 3. Physiological pulsatile inflow into the common carotid artery inlet over nondimensional duration of one cardiac cycle [49].

Holdsworth (1999) [49] and digitized in our laboratory [50–53]. The period of the waveform is 1 s, corresponding to a physiological pulse duration of 60 bpm.

Cell culture medium fluid properties are used, and the flow is Reynolds number matched to that of physiological blood flow. The choice of this fluid enables a more robust adaptation of flow results to experimental biological cell studies relying on those fluid dynamics studies to interpret observed cell mechanotransduction as a response to flow. Cell culture medium can be approximated as water in a standard cell study environment at 37 °C, due to its placement in incubators. Thus, the fluid has a kinematic viscosity of $6.95 \times 10^{-7} \mathrm{m}^2$ sec. Furthermore, as carotid artery flow experiences only minor non-Newtonian effects [54] a Newtonian fluid assumption is used.

Outlet boundary conditions at the ICA and ECA were resistive outflow boundary condition, due to their numerical robustness and almost identical behavior as a three-element Windkessel model [55]. Applying the resistive outlet boundary conditions instead of a Windkessel model reduced complexity. Systemic compliance effects, typically modeled by adding capacitors to the resistances (e.g., Windkessel model) were incorporated into the simulations via the inflow waveform developed by Holdsworth *et al.* [49]. The transient resistive outlet conditions are implemented using a user-defined-function (UDF), following the equation $\Delta p = R\,Q$, where Δp is the pressure drop in pascals, R is the vascular resistance in [$\mathrm{Pa\,s/m^3}$], and Q is the volume flow-rate in [$\mathrm{m^3/s}$]. The outlet pressure drop is controlled by the resistances and acts time-dependent due to its dependence on the inlet volume flow rate. Resistances are tuned iteratively to match clinical data of patient-averaged physiological mass outflows [56]. The ICA outlet boundary condition was set to represent this mass outflow matching clinical data, while ECA outflow was set as CCA inflow minus ICA outlfow. Resistances for the ICA and ECA are $R_{ICA} = 1.5 \times 10^6\,\mathrm{Pa\,s\,m^{-3}}$ and $R_{ECA} = 11 \times 10^6\,\mathrm{Pa\,s\,m^{-3}}$, respectively, for the healthy and disease-prone geometry.

For the unhealthy ΔP model, the healthy geometry model simulation was run with an increased ICA and decreased ECA outlet resistance according to Table II. This enables us to determine the

TABLE II. Resistances at ICA and ECA outlet boundary. The resistances in the Healthy column were applied to the healthy and disease-prone geometry. In the unhealthy ΔP geometry, conditions were achieved by applying the outlet resistances in the right column.

Resistance at outlet	Healthy	Unhealthy ΔP
R_{ICA} [$\mathrm{Pa\,s\,m^{-3}}$]	1.5×10^6	6.25×10^6
R_{ECA} [$\mathrm{Pa\,s\,m^{-3}}$]	11.0×10^6	6.25×10^6

effect of different mass flow and pressure gradient on vortical structures while holding the geometry constant, so within the same healthy geometry.

C. Identification and characterization of main vortical structures

The identification of three-dimensional vortical structures in the flow field will be performed using the λ_2 criterion, a widely used vortex identification technique [57] in cardiovascular fluid dynamics. Furthermore, a great advantage of this quantitative method is that it is based on the physical definition of the vortical structure and does not depend on the visualization technique [58]. The λ_2 criterion is a Eulerian and eigenvalue-based vortex identification method [59]. The three-dimensional velocity field $\vec{u} = (u, v, w)$ is used to calculate the velocity gradient tensor $\mathbf{J}$ following Eq. (1):

$$\mathbf{J} = \begin{bmatrix} \frac{\partial u}{\partial x} & \frac{\partial u}{\partial y} & \frac{\partial u}{\partial z} \\ \frac{\partial v}{\partial x} & \frac{\partial v}{\partial y} & \frac{\partial v}{\partial z} \\ \frac{\partial w}{\partial x} & \frac{\partial w}{\partial y} & \frac{\partial w}{\partial z} \end{bmatrix}. \tag{1}$$

This velocity gradient tensor is decomposed into the symmetric strain deformation tensor $\mathbf{S}$ Eq. (2) and the asymmetric rotation rate tensor $\boldsymbol{\Omega}$ Eq. (3) [58]:

$$\mathbf{S} = \frac{\mathbf{J} + \mathbf{J}^{\mathrm{T}}}{2}, \tag{2}$$

$$\boldsymbol{\Omega} = \frac{\mathbf{J} - \mathbf{J}^{\mathrm{T}}}{2}. \tag{3}$$

Eigenvalues of $(\mathbf{S}^2 + \boldsymbol{\Omega}^2)$ are computed, so that $\lambda_1 \geqslant \lambda_2 \geqslant \lambda_3$. A voxel is part of a vortex core if it has two negative eigenvalues, thus if $\lambda_2 < 0$. A vortex is defined as a connected regions of $\lambda_2 < 0$ voxels [58,60–62]. To visualize vortical structures a threshold of λ_2 can be applied [58], and λ_2 plots show the three-dimensional isosurfaces of the chosen λ_2 threshold. A Python code was developed for postprocessing to isolate and track key vortices. The vortex core is characterized as a local pressure minimum, and the precise location of the vortex was determined by monitoring a local pressure minimum. This enabled the analysis of the moment in time and location for vortex formation, as well as its evolution over the cardiac cycle. Details of the vortex tracking algorithm can be found in [39].

1. Identification of vortex core and boundary for circulation calculation

In addition to vortex visualization, the circulation of specific vortical structures is calculated to quantitatively compare the vortical structures in the different geometries. Vorticity contours alone do not provide a robust method to identify a connected vortex [63]. Graftieaux *et al.* [64] introduced a vortex identification method that calculates the vortex core and boundary based on the velocity field. Thus, this method overcomes the common difficulty of multiple maxima of the vortex core criterion that might be present in a single high-vorticity region [63]. In the criterion introduced by Graftieaux *et al.* [64] two scalar functions Γ_1 and Γ_2 are calculated based on the velocity field, where Γ_1 identifies the vortex core and Γ_2 the vortex boundary. These Γ_1 and Γ_2 vortex criteria are defined by Eqs. (4) and (5), respectively:

$$\Gamma_1(p) = \frac{1}{N} \sum_{i=1}^{N} \frac{((\mathbf{x_p} - \mathbf{x_i}) \times \mathbf{u_i}) \cdot \mathbf{n}}{\|\mathbf{x_p} - \mathbf{x_i}\| \cdot \|\mathbf{u_i}\|}, \tag{4}$$

$$\Gamma_2(p) = \frac{1}{N} \sum_{i=1}^{N} \frac{((\mathbf{x_p} - \mathbf{x_i}) \times (\mathbf{u_i} - \bar{\mathbf{u}}_\mathbf{p})) \cdot \mathbf{n}}{\|\mathbf{x_p} - \mathbf{x_i}\| \cdot \|\mathbf{u_i} - \bar{\mathbf{u}}_\mathbf{p}\|}. \tag{5}$$

The calculation of Γ_1 and Γ_2 is performed at any point p of the flow field. $\mathbf{x}$ and $\mathbf{u}$ are position and velocity vectors, $\mathbf{n}$ the unit vector in out-of-plane direction, and N the total number of points in a control volume. $\bar{\mathbf{u}}_\mathbf{p}$ is the average velocity based on this control volume. Γ_1 and Γ_2 are computed on every point within a specific region of interest, in our case the ICA sinus. The region of interest is limited to the sinus as results obtained previously show that the major vortical structure of interest is located in the ICA sinus. By limiting the region of interest in the vortex identification code, computational cost can be reduced and stable results be achieved. Γ_1 and Γ_2 have a maximum value of 1. A vortex core is typically characterized by $|\Gamma_1|$ greater then 0.9 and the vortex boundary is characterized by $|\Gamma_2|$ values greater than $\frac{2}{\pi}$ [63]. A region is classified as a vortex when the algorithm could detect a vortex core that is enclosed in a vortex boundary. A MATLAB algorithm was used for the Γ_1-Γ_2 vortex identification where a control volume of $N = 5$ around each point p, and $|\Gamma_1|$ and $|\Gamma_2|$ thresholds of 0.7 and $\frac{2}{\pi}$ were used.

To facilitate this vortex identification algorithm, the three-dimensional CFD data, which were originally obtained on an unstructured grid, were interpolated onto a structured grid. The vortex identification and following calculation of the main vortex circulation are performed in the two-dimensional center plane, at $z = 0$. The circulation Γ of the vortex is calculated by integrating the vorticity over the area within the defined vortex boundary; see Eq. (6) (A_v describes the vortex area located inside the vortex boundary determined by the Γ_2 criterion):

$$\Gamma = \oint_C \mathbf{u} \cdot d\mathbf{r} = \iint_{A_v} (\nabla \times \mathbf{u}) \cdot d\mathbf{A_v}. \tag{6}$$

III. RESULTS

This section will detail the resulting disease-prone conditions achieved in a healthy geometry. A quantification of flow split as well as internal carotid artery sinus axial pressure gradient for our conditioned geometry will be provided, in comparison with the previously studied [38,39] healthy and disease-prone geometries. Further, the effect of the conditioning on the lifespan of the sinus hairpin vortical structure will be elaborated. In the following sections, the successful detection of the main vortices in the sinus using the Γ-1-Γ-2 method will be shown, as well as calculations of their circulation.

A. Disease-prone conditions in healthy geometry

The unhealthy ΔP simulation recreated conditions within the healthy geometry that resemble those present in the disease-prone case. This is done by increasing the ICA and decreasing the ECA outlet resistance. This directly impacts the flow split between ICA and ECA and thus the mass outflow through the two branches. As Fig. 4 shows, geometric difference alone, and thus changed flow resistance due solely to geometry, between healthy and disease-prone geometry causes a significant difference in outlet mass flow. The change in outlet resistances for the unhealthy ΔP case closely replicates the flow split percentages of a disease-prone environment within the healthy geometry.

This study allows us to isolate effects caused by the geometry vs those caused by the axial pressure gradient and thus to investigate the effect of the axial pressure gradient acting over the ICA sinus on the vortex ring lifespan. Via modified outlet resistances, an axial pressure gradient closely replicating the disease-prone pressure levels could be achieved in a healthy geometry as shown in Fig. 5.

B. Pressure-gradient effect on hairpin vortexlifespan

The hairpin vortex is tracked by its vortex core that imprints a pressure minimum at the sinus side wall. Results of vortex lifespan are compared between the healthy, the disease-prone, and the unhealthy ΔP models, shown in blue, red, and green in Fig. 6, respectively. When creating

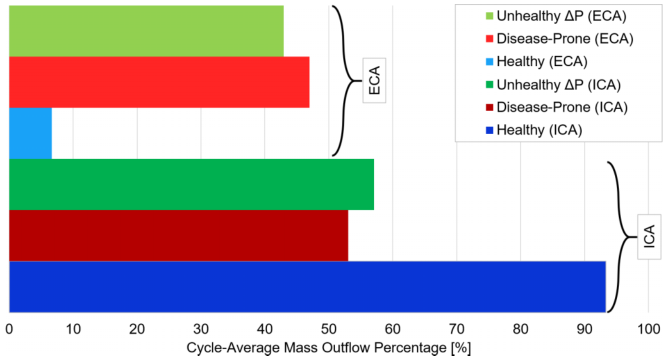

FIG. 4. Mass outflow percentage of total inflow, averaged over one flow cycle for the ICA and ECA, respectively. Healthy geometry is shown in blues, disease-prone in reds, and unhealthy ΔP in greens.

disease-prone flow conditions (mass outflow rate and axial pressure gradient) within the healthy geometry—thus the unhealthy ΔP model—the hairpin vortex forms at almost the same moment in time as in the healthy case. In addition, the hairpin vortex follows almost the same downstream trajectory. This shows that the moment and downstream location of hairpin vortex formation are determined by geometry. The hairpin vortical structure, however, does decay (fall under the λ_2 threshold) significantly earlier under the disease-prone pressure conditions within the healthy geometry. In the regular healthy geometry, the hairpin vortical structure is detected during approximately 75% of the cycle, whereas in the disease-prone geometry it is present for about 25% of the cycle, and formed sooner in the cycle. Even though in the unhealthy ΔP model the moment of formation closely matches the one in the healthy geometry, its lifespan is nearly the same as the disease-prone model with about 27% of the cycle (compare the onset and duration of the green and blue curves in Fig. 6). Thus, we conclude that the lifespan of the vortex, which depends on its rate of decay, is dominated by axial pressure gradient effects and not by the geometry.

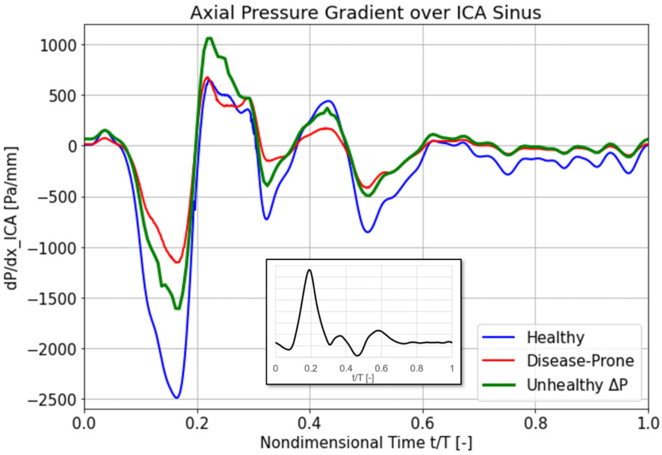

FIG. 5. Axial pressure gradient acting over the ICA sinus per sinus length is plotted over the nondimensional time (t/T) duration of one flow cycle. Healthy geometry is shown in blue, disease-prone in red, and unhealthy ΔP in green.

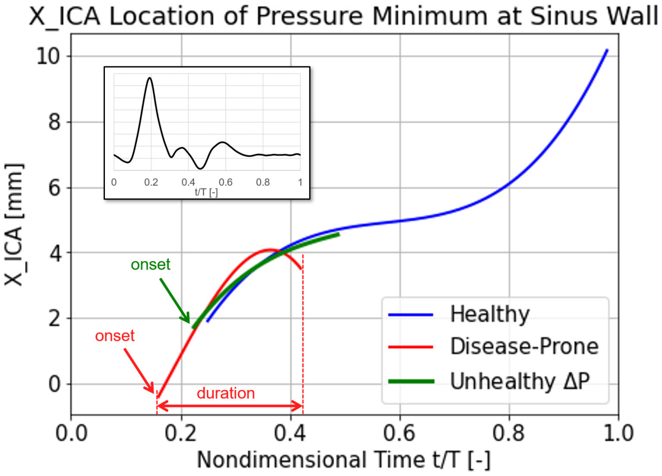

FIG. 6. Location of hairpin vortical structure core along the axial ICA sinus direction, over one cycle ($T = 1$ sec). Healthy geometry is shown in blue, disease-prone in red, and unhealthy ΔP in green.

C. Circulation of hairpin vortical structure

This section quantifies the evolution of the dominant vortex over one cardiac cycle. It shows the identification of vortex boundary and vortex core over time. Total circulation of this detected vortex and its spatial evolution will be discussed.

1. Vortex Identification using Γ_1-Γ_2 *Method*

The goal of the using Γ_1-Γ_2 method is to identify robustly the main vortex in the critical internal carotid artery sinus region. This algorithm detects the vortex based on vorticity, thus the results of the vortex identification are shown in Fig. 7. A two-dimensional plane at the vessel's center is shown for the unhealthy ΔP geometry at 21 moments in the cardiac cycle. Vorticity is shown in blue-white-red color contours. The Γ_1-Γ_2 method detects the boundary of a vortex as well as the core of a vortex, where they are shown by a green line and cross, respectively. The total area of the main detected vortex is filled with a slight transparent green color. A feature is identified as a vortex only when the vortex core lies inside a boundary.

Figure 7 clearly illustrates the periodic behavior over cardiac cycles as the vorticity plot and vortex identification exhibit almost identical results at time $t/T = 0.02$ and $t/T = 1.0$, which correspond to the beginning and end of the cardiac cycle, respectively. The vortex that is identified at $t/T = 0.02$ is not detected at subsequent times ($t/T = 0.05$, $t/T = 0.1$), indicating that this is a vortex from the previous cardiac cycle. Referring to the second row, starting at $t/T = 0.15$, another vortex is detected again. It is the first vortex that was formed in this cardiac cycle, called the systolic phase vortex herein. Over time it moves slightly upstream, as well as towards the outer sinus wall. It is detected between $t/T = 0.15$ and $t/T = 0.4$, which agrees with the time interval of the lifespan of the main hairpin vortex, which was not detected in the second half of the cycle. Our previous studies found that this main hairpin vortex induces healthy levels of wall-shear stresses on the outer sinus wall, the critical location for plaque formation, and thus has a physiological beneficial role. In Fig. 7 in the time interval from $t/T = 0.15$ to $t/T = 0.4$ we can observe that this vortex indeed moves slightly upstream over time but, most importantly, always stays very close to the outer sinus wall.

At $t/T = 0.55$ another vortex is detected by the algorithm, having a different shape and position than the early cycle main hairpin vortex. This diastolic phase vortex has very high vorticity values and forms close to the outer sinus wall. This diastolic phase vortex grows in size very quickly and is

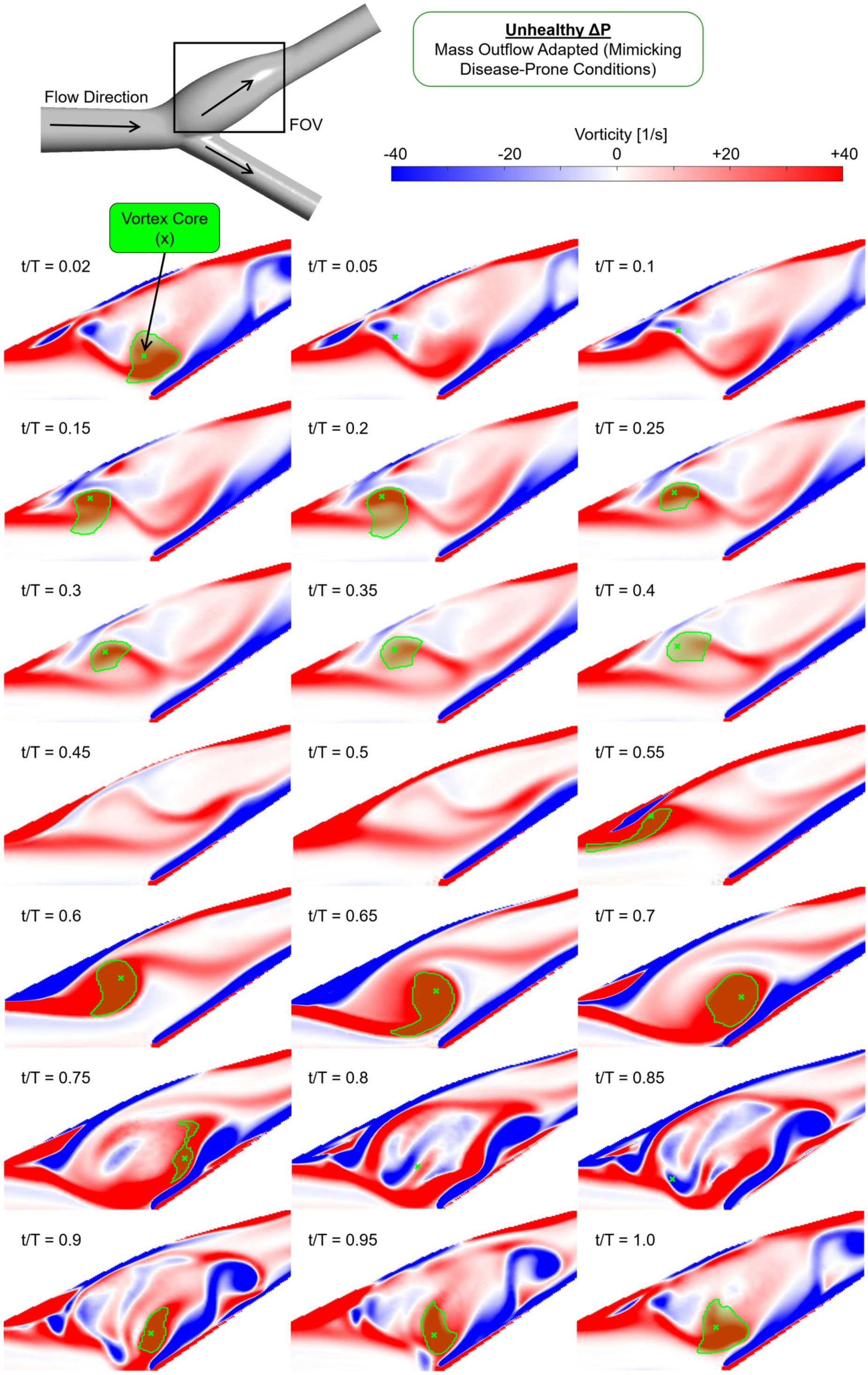

FIG. 7. Vorticity contours on the ICA sinus center plane for the unhealthy ΔP geometry at 21 moments in the flow cycle. Vortex core and boundary identified by the Γ-1-Γ-2 method are indicated in bright green for each time frame.

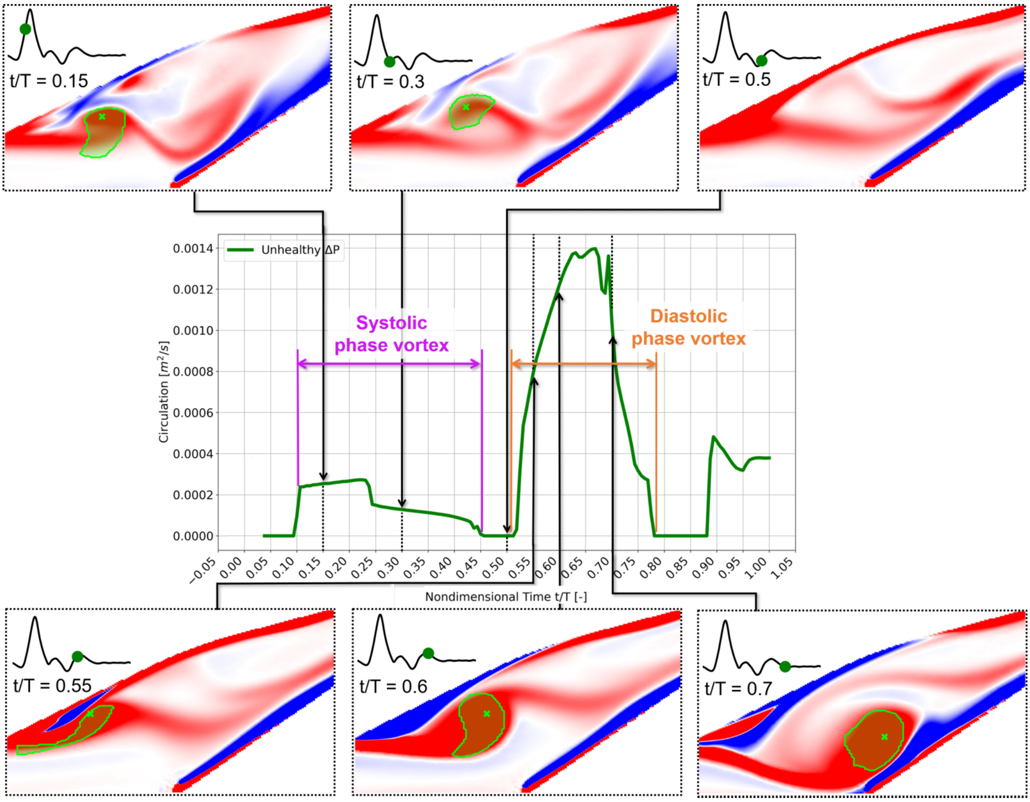

FIG. 8. Center: Circulation of unhealthy ΔP geometry as lineplot over one nondimensionalized flow cycle. Six insets with the vorticity contours withing the internal carotid artery sinus of the unhealthy ΔP geometry as well as the boundary and core of the detected vortex highlighted in bright green surrounding. The arrows onto the lineplot and the "$t/T =$ label" as well as the green dot on the waveform within the inset show moment in time of respective inset.

detected until $t/T = 0.75$. Between $t/T = 0.65$ and $t/T = 0.7$ this vortex appears to impinge on the sinus inside wall and strongly deforms, as can be seen at $t/T = 0.75$. Consequently, the high-vorticity regions in subfigures $t/T = 0.8$ and $t/T = 0.85$ no longer form a coherent structure, thus no vortex is detected. This diastolic phase vortexcreates a vorticity field with strong positive and negative local variations, which mirrors the oberservation of disturbed flow with additional strong but small vortical structures in the second half of the cycle, as described in [39]. This figure also clearly showcases the effect of threshold change on the results. When comparing the detected vortex area between $t/T = 0.65$ and $t/T = 0.7$, the vortex area decreased as the vortex loses its "tail," which has fallen below the defined threshold, whereas the vorticity plots seem very similar. In addition, from $t/T = 0.9$ to $t/T = 1.0$ the algorithm picks up the diastolic phase vortex again, after the disturbances and large jumps between positive and negative vorticity are reduced over time. The moment of formation of the systolic phase vortex and diastolic phase vortex coincide with the acceleration portion of the inflow waveform during systole and diastole, respectively.

Figure 8 shows at six important instants of the cardiac cycle vorticity contours within the internal carotid artery sinus of the unhealthy ΔP geometry as well as the boundary and core of the detected vortex highlighted in green, just as described in Fig. 7. In addition to the nondimensional times (t/T) the inset on the top left of these plots shows the moment in time within the cycle indicated by a green dot on the black waveform. In the middle, a lineplot shows the calculated circulation

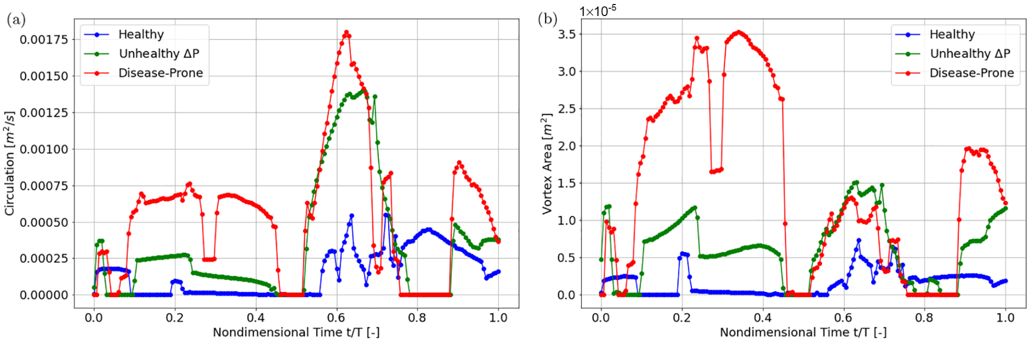

FIG. 9. Circulation and vortex are of main vortex detected using Γ_{-1}-Γ_{-2} method over the nondimensional time duration of one cycle. Healthy geometry is shown in blue, disease-prone in red, and unhealthy ΔP in green. (a) Circulation of dominant vortex within vortex boundary. (b) Area of dominant vortex within boundary.

within the detected vortex area, over the nondimensional time of one cardiac cycle with period $T = 1$ s. The circulation shows the same pattern as the vortex detection. The vortex detected and its corresponding circulation before $t/T = 0.05$ is an vortex created in the previous cardiac cycle, which weakens rapidly. The circulation lineplot shows that the systolic phase vortex builds strength initially and then slowly decays in strength until it is not detected anymore around $t/T = 0.45$. It also clearly shows that the diastolic phase vortex is much stronger, as its peak circulation magnitude is roughly 4.5 times the maximum circulation of the systolic phase vortex. Its circulation peaks only very briefly as around $t/T = 0.65$ its circulation decays rapidly. This instant of rapid circulation decline coincides with the vortex's impingement on the inner sinus wall as discussed before.

2. *Circulation over time for healthy, disease-prone, and unhealthy* **ΔP** *geometries*

The main vortex was identified for all three cases, healthy, disease-prone, and unhealthy ΔP, as discussed above. The detection of the boundary can then be used to calculate the area of the cross section of the vortex, which is representative of the area it occupies within the sinus. The area is calculated within the detected vortex boundary and plotted in Fig. 9(b), which shows the vortex area vs the nondimensional time (t/T) over one cardiac cycle. The circulation of the main vortex is determined within the detected vortex boundary using Eq. (6). The calculated circulation of the detected vortex over the nondimensional time (t/T) is shown in Fig. 9(a). In both plots the healthy geometry is shown in blue, the disease-prone in red, and the unhealthy ΔP in green. When considering the circulation plot [Fig. 9(a)], the aforementioned two vortices can be observed for all three geometries as the circulation dips to zero around $t/T = 0.5$ indicating the absence of the decayed systolic phase vortex. The diastolic phase vortex has a significantly higher circulation than the systolic phase vortex in all three cases. Considering the healthy geometry, the vortex is first detected (has nonzero circulation) around $t/T = 0.2$, whereas for the disease-prone and unhealthy ΔP geometry the vortex circulation increases (is being detected) earlier at around $t/T = 0.15$. This is in agreement with the moment of formation found with the previous analysis of main hairpin vortex lifespan. Especially for the systolic phase vortex ($t/T < 0.5$), the circulation of the disease-prone geometry is the highest, while for the healthy case it is weakest. The circulation for the disease-prone case falls in between, following the same shift pattern as the axial pressure gradient in the sinus observed before. Considering the area the vortex occupies [Fig. 9(b)], it is obvious that the systolic phase vortex occupies the largest area in the disease-prone geometry. A notable observation is that the vortex in the unhealthy ΔP case has a relatively small area, more similar to the healthy geometry than to the disease-prone geometry. This highlights the influence of the sinus expansion on the size of this systolic phase vortex, as the maximum sinus diameter is about 20% larger in the disease-prone case. Second, differences in area of the early cycle vs the late cycle vortex

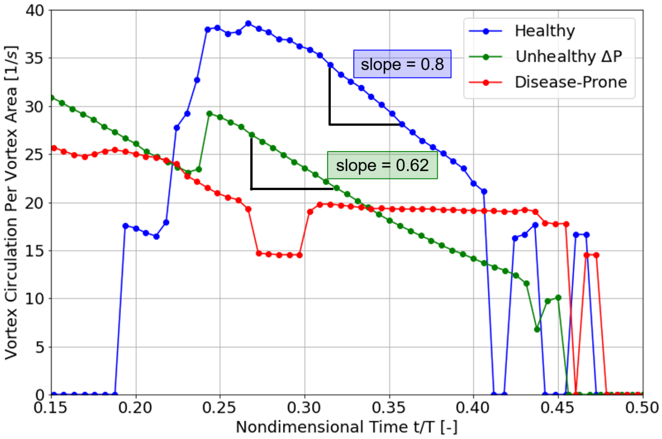

FIG. 10. Circulation of systolic phase vortex vortex divided by its area, as defined in Fig. 9. Healthy geometry is shown in blue, disease-prone in red, and unhealthy ΔP in green.

can be observed among the three geometries. In the disease-prone geometry, the systolic phase vortex is significantly larger than the diastolic phase vortex, whereas for the healthy and unhealthy ΔP geometry, the diastolic phase vortex occupies a slightly larger area than the systolic phase vortex. The size of the vortex strongly depends on the sinus volume. For better comparison between the cases the circulation per vortex area will be analyzed in the following (Fig. 10). The difference of moment of formation is confirmed again, as the vortex in the disease-prone and unhealthy ΔP geometry forms earlier, versus it only forms around $t/T = 0.2$ for the healthy case. We can make several key observations when comparing geometries. First, the circulation per vortex area decreases nearly linearly for the healthy as well as the unhealthy ΔP geometry shortly after detection until the point it deteriorates (falls under the detection threshold) at around $t/T = 0.44$ for the unhealthy ΔP case. Both cases have similar slopes, from which we conclude that their decay is mainly controlled by the geometry (pressure gradient), as both cases are the same geometric model. On the other hand, in the disease-prone case, the circulation per vortex area remains at a nearly constant level soon after formation. Despite its negative slope with time the healthy geometries' circulation per vortex area value stays above the value of the disease-prone geometry. The circulation per vortex area value for the unhealthy ΔP geometry, on the other hand, falls below the disease-prone line at around $t/T = 0.33$ as it is shifted to lower values by a constant offset compared to the healthy geometries results.

3. *Circulation and three-dimensional vortical structure in healthy-increased-$\mathbf{R}_{\mathrm{ICA}}$ geometry*

Similar to Fig. 8, in the center of Fig. 11 the circulation of the identified vortex in the internal carotid artery sinus of the unhealthy ΔP geometry is shown over the duration of one cycle. The line is colored by its circulation magnitude, red being the highest circulation, and violet the lowest circulation, as indicated by the color bar on the right of the line plot. Again, six insets corresponding to six moments in the cycle are lined on the top and bottom. These insets show three-dimensional results, where the vessel wall is colored by a half transparent gray. The nondimensional times (t/T) are indicated with dots on the inflow waveform shown in the inset on the middle right. Point colors correspond to the color of the respective frame of the three-dimensional subfigure. On the inside, three-dimensional vortical structures are shown using a λ_2 criterion threshold. The coherent vortical structure in three dimensions is then uniformly colored by the respective circulation value. The systolic phase vortex, the main hairpin vortex, can be clearly identified in the first half of the cycle as a single vortex. In the second half of the cycle, the stronger diastolic phase vortex dominates, and this figure clearly shows that with the formation of this diastolic phase vortex multiple vortices are detected by the λ_2 criterion threshold. Another interesting observation is revealed in the waveform

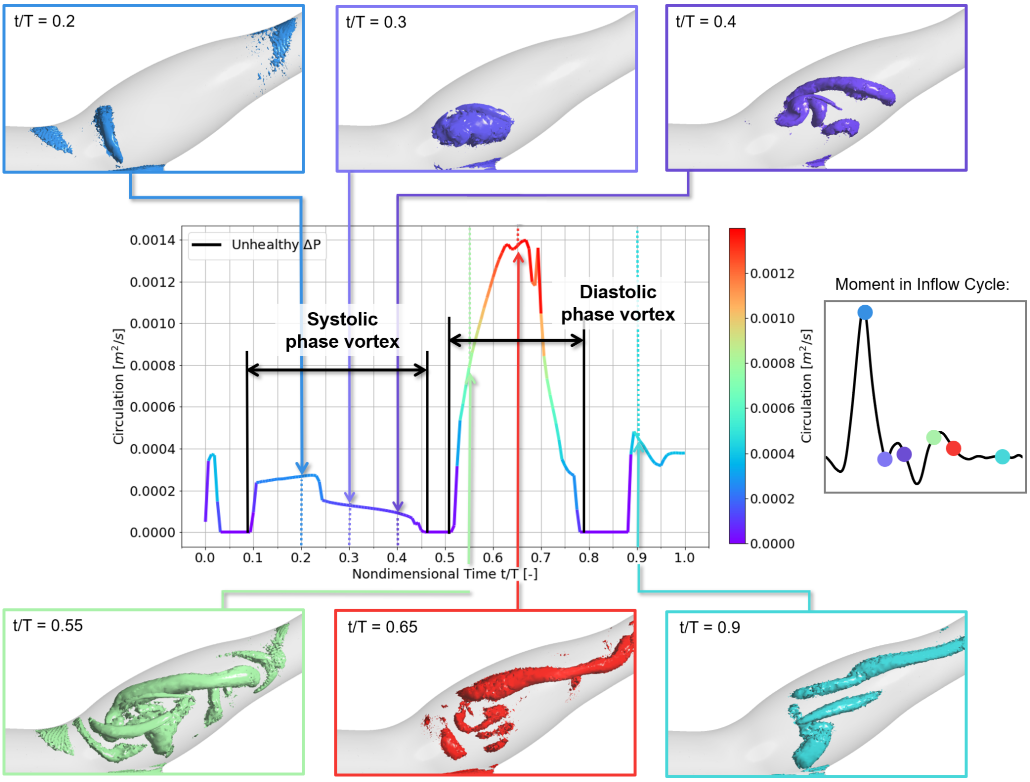

FIG. 11. Lineplot: Circulation of identified vortex using Γ_1-Γ_2-method for unhealthy ΔPgeometry, line colored using rainbow colorbar corresponding to respective circulation magnitude. Surrounding three-dimensional plots show the three-dimensional vortical structure using a λ_2 threshold of 0.08 colored corresponding to the respective circulation value.

inset on the middle right. As described before, it shows the moments of time of the six representative three-dimensional plots as dots that are colored with the respective circulation magnitude of the dominant vortex. Circulation values are highest after $t/T = 0.55$, i.e., around the second inflow velocity peak, which is in the diastolic phase of the cycle. Circulation of this diastolic phase vortex is high at $t/T = 0.55$ and increases to peak around $t/T = 0.65$ as the inflow decelerates before circulation decays over time until the end of the cardiac cycle.

IV. CONCLUSION

The aim of this study is to elucidate the underlying flow physics driving vortical structure behavior in the carotid artery bifurcation and its role in establishing pathological pro-atherogenic wall-shear-stress distributions. Our previous studies found a main vortical structure in the carotid artery sinus and increased the fundamental understanding of vortex evolution over the cardiac cycle, enabling the characterization of differences between healthy physiological and pathological vortical structures. In this study, we correlate changes in flow split and axial pressure gradient over the ICA sinus to pro-atherogenic vortex behavior with the goal of prospective transfer into clinical early detection methods of atherosclerosis risk. In addition to our previously developed patient-averaged healthy and disease-prone carotid artery bifurcation models, a developed model consisting of healthy geometry with flow conditions mimicking those in a disease-prone geometry, called unhealthy ΔP, was introduced. In this model, the ICA outlet resistance was increased, and the

ECA outlet resistance decreased, respectively. This change in outlet resistances created a mass flow split very similar to the one present in a disease-prone CAB, but within a CAB geometry with healthy anatomical features. In addition, the axial pressure gradient peak over the ICA sinus approached disease-prone levels around the time of hairpin vortex formation. By tracking hairpin vortex lifespan, we concluded that the time of vortex formation is defined by the geometry as the vortex in the healthy and unhealthy ΔPgeometry formed around the same time in the cycle. The lifespan (rate of decay) of the vortex, however, is dominated by the flow conditions (mass-flow split and axial pressure gradient), as the disease-prone and unhealthy ΔP geometry experienced a similar vortex lifespan of around 25% of the cardiac cycle, whereas the vortex in the healthy geometry persisted for almost 75% of the cardiac cycle. Circulation calculations revealed the existences of two main vortices, with the systolic phase vortex matching the tracked hairpin vortical structure. This systolic phase vortex advects downstream over time, and most importantly, towards the sinus outer wall. This allows it to significantly increase wall-shear stresses in the outer sinus wall as reported in [39]. The diastolic phase vortex has much higher circulation, but due to its motion towards the ICA inner wall and away from the critical ICA sinus outer wall, has less effect on the wall-shear stresses in this critical region. The size (reported vortex cross-sectional area) of the systolic phase vortex and the time-dependent decay of the circulation per vortex area are dominated by the geometry.

This study indicates that the carotid artery bifurcation geometry is responsible for the vortical structure behavior; the flow conditions, in terms of mass flow split and sinus axial pressure gradient, are, however, what dominate the critical hairpin vortex's lifespan. As identified in our earlier study, this pathological shortened vortical structure lifespan is likely to be the disadvantageous cause for a pro-atherogenic wall-shear-stress distribution underlying disease formation. Thus, we conclude that the deviation from characteristic healthy flow conditions, namely, a high ICA mass flow rate and a higher initial favorable pressure gradient peak, is potentially a strong indicator for predisposition towards development of atherosclerosis. Correlating a single quantity, such as the high ICA mass flow rate, to pro-atherogenic conditions is a promising tool to serve as a decision-making factor for future clinical early detection of atherosclerosis risk.

ACKNOWLEDGMENTS

This research was supported by the National Science Foundation, Biomechanics & Mechanobiology (BMMB) Program, under Grant No. CMMI-1854415. N.C.W. was further supported by the George Washington University graduate research assistantship and the Michael K. Myers Merit Scholarship. This study was completed in part with resources provided by the High-Performance Computing Cluster at The George Washington University, Information Technology, Research Technology Services.

---

[1] K. B. Chandran, S. E. Rittgers, and A. P. Yoganathan, *Biofluid Mechanics: The Human Circulation* (CRC Press, 2012).

[2] Advanced Vascular Surgery, Tcar (carotid revascularization), https://www.avsurgery.com/services/tcar-carotidrevascularization/ (2022).

[3] Mayfield Brain and Spine, Carotid stenosis (carotid artery disease), https://www.avsurgery.com/service/carotid-artery-disease (2023).

[4] J.-J. Chiu, D. L. Wang, S. Chien, R. Skalak, and S. Usami, Effects of disturbed flow on endothelial cells, ASME Ann. Biomed. Eng. **120**, 2 (1998).

[5] G. Dai, M. R. Kaazempur-Mofrad, S. Natarajan, Y. Zhang, S. Vaughn, B. R. Blackman, R. D. Kamm, G. García-Cardeña, and M. A. Gimbrone Jr., Distinct endothelial phenotypes evoked by arterial waveforms derived from atherosclerosis-susceptible and-resistant regions of human vasculature, Proc. Natl. Acad. Sci. USA **101**, 14871 (2004).

[6] Y.-C. Fung, *Biomechanics: Circulation* (Springer Science & Business Media, 2013).

[7] S. Y. Hann, H. Cui, N. C. Zalud, T. Esworthy, K. Bulusu, Y.-L. Shen, M. W. Plesniak, and L. G. Zhang, An *in vitro* analysis of the effect of geometry-induced flows on endothelial cell behavior in 3D printed small-diameter blood vessels, Biomater. Adv. **137**, 212832 (2022).

[8] N. C. Zalud, K. Bulusu, and M. Plesniak, Simulation of a pro-atherogenic high-risk carotid artery bifurcation geometry, Bull. Am. Phys. Soc. **67**, U05.00003 (2022).

[9] A. S. French, Mechanotransduction, Annu. Rev. Physiol. **54**, 135 (1992).

[10] J. M. Tarbell, S. Weinbaum, and R. D. Kamm, Cellular fluid mechanics and mechanotransduction, Ann. Biomed. Eng. **33**, 1719 (2005).

[11] H. A. Himburg, D. M. Grzybowski, A. L. Hazel, J. A. LaMack, X.-M. Li, and M. H. Friedman, Spatial comparison between wall shear stress measures and porcine arterial endothelial permeability, Am. J. Physiol.-Heart Circul. Physiol. **286**, H1916 (2004).

[12] K. M. Barber, A. Pinero, and G. A. Truskey, Effects of recirculating flow on u-937 cell adhesion to human umbilical vein endothelial cells, Am. J. Physiol.-Heart Circul. Physiol. **275**, H591 (1998).

[13] D. E. Conway, M. R. Williams, S. G. Eskin, and L. V. McIntire, Endothelial cell responses to atheroprone flow are driven by two separate flow components: Low time-average shear stress and fluid flow reversal, Am. J. Physiol.-Heart Circul. Physiol. **298**, H367 (2010).

[14] J. Ravensbergen, J. W. Ravensbergen, J. K. B. Krijger, B. Hillen, and H. W. Hoogstraten, Localizing role of hemodynamics in atherosclerosis in several human vertebrobasilar junction geometries, Arteriosclerosis Thrombosis Vascular Biol. **18**, 708 (1998).

[15] L. Rouleau, M. Farcas, J.-C. Tardif, R. Mongrain, and R. L. Leask, Endothelial cell morphologic response to asymmetric stenosis hemodynamics: Effects of spatial wall shear stress gradients, J. Biomech. Eng. **132**, 081013 (2010).

[16] D. Lopes, H. Puga, J. Teixeira, and R. Lima, Blood flow simulations in patient-specific geometries of the carotid artery: A systematic review, J. Biomech. **111**, 110019 (2020).

[17] A. D. Augst, B. M. C. G. Ariff, S. A. G. McG Thom, X. Y. Xu, and A. D. Hughes, Analysis of complex flow and the relationship between blood pressure, wall shear stress, and intima-media thickness in the human carotid artery, Am. J. Physiol.-Heart Circul. Physiol. **293**, H1031 (2007).

[18] C.-H. Li, B.-L. Gao, J.-W. Wang, J.-F. Liu, H. Li, and S.-T. Yang, Hemodynamic factors affecting carotid sinus atherosclerotic stenosis, World Neurosurg. **121**, e262 (2019).

[19] D. Lopes, H. Puga, J. C. Teixeira, and S. F. Teixeira, Influence of arterial mechanical properties on carotid blood flow: Comparison of CFD and FSI studies, Int. J. Mech. Sci. **160**, 209 (2019).

[20] U. Morbiducci, D. Gallo, D. Massai, R. Ponzini, M. A. Deriu, L. Antiga, A. Redaelli, and F. M. Montevecchi, On the importance of blood rheology for bulk flow in hemodynamic models of the carotid bifurcation, J. Biomech. **44**, 2427 (2011).

[21] X. Zhou, L. Yin, L. Xu, and F. Liang, Non-periodicity of blood flow and its influence on wall shear stress in the carotid artery bifurcation: An in vivo measurement-based computational study, J. Biomech. **101**, 109617 (2020).

[22] H. Bouteloup, J. G. de Oliveira Marinho, and D. M. Espino, Computational analysis to predict the effect of pre-bifurcation stenosis on the hemodynamics of the internal and external carotid arteries, J. Mech. Eng. Sci. **14**, 7029 (2020).

[23] F. J. H. Gijsen, F. N. van de Vosse, and J. D. Janssen, The influence of the non-Newtonian properties of blood on the flow in large arteries: Steady flow in a carotid bifurcation model, J. Biomech. **32**, 601 (1999).

[24] N. Kumar, S. M. Abdul Khader, R. Pai, S. H. Khan, and P. A. Kyriacou, Fluid structure interaction study of stenosed carotid artery considering the effects of blood pressure, Int. J. Eng. Sci. **154**, 103341 (2020).

[25] K. Perktold, M. Resch, and R. O. Peter, Three-dimensional numerical analysis of pulsatile flow and wall shear stress in the carotid artery bifurcation, J. Biomech. **24**, 409 (1991).

[26] D. N. Ku, D. P. Giddens, C. K. Zarins, and S. Glagov, Pulsatile flow and atherosclerosis in the human carotid bifurcation. Positive correlation between plaque location and low oscillating shear stress, Arteriosclerosis **5**, 293 (1985).

[27] K. T. Nguyen, C. D. Clark, T. J. Chancellor, and D. V. Papavassiliou, Carotid geometry effects on blood flow and on risk for vascular disease, J. Biomech. **41**, 11 (2008).

[28] C. F. Dewey, Dynamics of arterial flow, Adv. Exp. Med. Biol. **115**, 55 (1979).

[29] D. P. Giddens, C. K. Zarins, and S. Glagov, Response of arteries to near-wall fluid dynamic behavior, Appl. Mech. Rev. **43**, S98 (1990).

[30] R. M. Nerem, Vascular fluid mechanics, the arterial wall, and atherosclerosis, J. Biomech. Eng. **114**, 274 (1992).

[31] C. Cox, M. R. Najjari, and M. W. Plesniak, Three-dimensional vortical structures and wall shear stress in a curved artery model, Phys. Fluids **31**, 121903 (2019).

[32] Y. Chen, X. Yang, A. J. Iskander, and P. Wang, On the flow characteristics in different carotid arteries, Phys. Fluids **32**, 101902 (2020).

[33] A. Goddi, M. Fanizza, C. Bortolotto, M. V. Raciti, I. Fiorina, X. He, Y. Du, and F. Calliada, Vector flow imaging techniques: An innovative ultrasonographic technique for the study of blood flow, J. Clin. Ultrasound **45**, 582 (2017).

[34] M. S. M. Elbaz, E. E. Calkoen, J. J. M. Westenberg, B. P. F. Lelieveldt, A. A. W. Roest, and R. J. Van Der Geest, Vortex flow during early and late left ventricular filling in normal subjects: Quantitative characterization using retrospectively-gated 4D flow cardiovascular magnetic resonance and three-dimensional vortex core analysis, J. Cardiovasc. Magn. Reson. **16**, 78 (2014).

[35] M. S. M. Elbaz, R. J. van der Geest, E. E. Calkoen, A. de Roos, B. P. F. Lelieveldt, A. A. W. Roest, and J. J. M. Westenberg, Assessment of viscous energy loss and the association with three-dimensional vortex ring formation in left ventricular inflow: In vivo evaluation using four-dimensional flow MRI, Magn. Reson. Med. **77**, 794 (2017).

[36] A. Goddi, C. Bortolotto, M. V. Raciti, I. Fiorina, L. Aiani, G. Magistretti, A. Sacchi, C. Tinelli, and F. Calliada, High–frame rate vector flow imaging of the carotid bifurcation in healthy adults: Comparison with color Doppler imaging, J. Ultrasound Med. **37**, 2263 (2018).

[37] S. W. Youn and J. Lee, From 2D to 4D phase-contrast MRI in the neurovascular system: Will it be a quantum jump or a fancy decoration? J. Magn. Reson. Imaging **55**, 347 (2022).

[38] N. C. Zalud, K. V. Bulusu, and M. W. Plesniak, Shear stress metrics associated with pro-atherogenic high-risk anatomical features in a carotid artery bifurcation model, Clin. Biomech. **105**, 105956 (2023).

[39] N. C. Wild, K. V. Bulusu, and M. W. Plesniak, Vortical structures promote atheroprotective wall shear stress distributions in a carotid artery bifurcation model, Bioeng. **10**, 1036 (2023).

[40] N. C. Wild, K. Bulusu, and M. Plesniak, The role of vortical structures and axial pressure gradients in promoting atheroprotective wall-shear-stress distributions in carotid artery models, Bull. Am. Phys. Soc. **A10**, A10.00005 (2023).

[41] L. Goubergrits, K. Affeld, J. Fernandez-Britto, and L. Falcon, Geometry of the human common carotid artery. A vessel cast study of 86 specimens, Pathol.-Res. Practice **198**, 543 (2002).

[42] I. Marshall, P. Papathanasopoulou, and K. Wartolowska, Carotid flow rates and flow division at the bifurcation in healthy volunteers, Physiol. Meas. **25**, 691 (2004).

[43] S. Tada and J. M. Tarbell, A computational study of flow in a compliant carotid bifurcation–stress phase angle correlation with shear stress, Ann. Biomed. Eng. **33**, 1202 (2005).

[44] T. G. Phan, R. J. Beare, D. Jolley, G. Das, M. Ren, K. Wong, W. Chong, M. D. Sinnott, J. E. Hilton, and V. Srikanth, Carotid artery anatomy and geometry as risk factors for carotid atherosclerotic disease, Stroke **43**, 1596 (2012).

[45] K. Spanos, G. Petrocheilou, C. Karathanos, N. Labropoulos, D. Mikhailidis, and A. Giannoukas, Carotid bifurcation geometry and atherosclerosis, Angiology **68**, 757 (2017).

[46] J. B. Thomas, L. Antiga, S. L. Che, J. S. Milner, D. A. H. Steinman, J. D. Spence, B. K. Rutt, and D. A. Steinman, Variation in the carotid bifurcation geometry of young versus older adults: Implications for geometric risk of atherosclerosis, Stroke **36**, 2450 (2005).

[47] C. Cox, Development of a high-order Navier-Stokes solver using flux reconstruction to simulate three-dimensional vortex structures in a curved artery model, Ph.D. thesis, The George Washington University, 2018.

[48] C. Poelma, P. N. Watton, and Y. Ventikos, Transitional flow in aneurysms and the computation of haemodynamic parameters, J. R. Soc. Interface **12**, 20141394 (2015).

[49] D. W. Holdsworth, C. J. D. Norley, R. Frayne, D. A. Steinman, and B. K. Rutt, Characterization of common carotid artery blood-flow waveforms in normal human subjects, Physiol. Meas. **20**, 219 (1999).

[50] K. V. Bulusu and M. W. Plesniak, Secondary flow morphologies due to model stent-induced perturbations in a 180 curved tube during systolic deceleration, Exp. Fluids **54**, 1493 (2013).

[51] A. L. Glenn, K. V. Bulusu, F. Shu, and M. W. Plesniak, Secondary flow structures under stent-induced perturbations for cardiovascular flow in a curved artery model, Int. J. Heat Fluid Flow **35**, 76 (2012).

[52] M. R. Najjari and M. W. Plesniak, Evolution of vortical structures in a curved artery model with non-Newtonian blood-analog fluid under pulsatile inflow conditions, Exp. Fluids **57**, 1 (2016).

[53] S. D. Peterson and M. W. Plesniak, The influence of inlet velocity profile and secondary flow on pulsatile flow in a model artery with stenosis, J. Fluid Mech. **616**, 263 (2008).

[54] J. Boyd and J. M. Buick, Comparison of Newtonian and non-Newtonian flows in a two-dimensional carotid artery model using the lattice Boltzmann method, Phys. Med. Biol. **52**, 6215 (2007).

[55] F. Capuano, Y.-H. Loke, and E. Balaras, Blood flow dynamics at the pulmonary artery bifurcation, Fluids **4**, 190 (2019).

[56] M. D. Ford, N. Alperin, S. H. Lee, D. W. Holdsworth, and D. A. Steinman, Characterization of volumetric flow rate waveforms in the normal internal carotid and vertebral arteries, Physiol. Meas. **26**, 477 (2005).

[57] A. Kheradvar, G. Pedrizzetti, A. Kheradvar, and G. Pedrizzetti, *Vortex Formation in the Heart* (Springer, 2012).

[58] M. S. M. ElBaz, B. P. F. Lelieveldt, J. J. M. Westenberg, and R. J. Van Der Geest, Automatic extraction of the 3D left ventricular diastolic transmitral vortex ring from 3D whole-heart phase contrast MRI using Laplace-Beltrami signatures, in *Statistical Atlases and Computational Models of the Heart. Imaging and Modelling Challenges: 4th International Workshop, STACOM 2013, Held in Conjunction with MICCAI 2013, Nagoya, Japan, September 26, 2013*, Revised Selected Papers 4 (Springer, 2014), pp. 204–211.

[59] Y. Gao and C. Liu, Rortex and comparison with eigenvalue-based vortex identification criteria, Phys. Fluids **30**, 085107 (2018).

[60] J. Ahrens, B. Geveci, C. Law, C. D. Hansen, and C. R. Johnson, Visualization handbook, in *ParaView: An End-User Tool for Large Data Visualization* (Elsevier Cambridge, MA, 2005), pp. 717–731.

[61] Q. Chen, Q. Zhong, M. Qi, and X. Wang, Comparison of vortex identification criteria for planar velocity fields in wall turbulence, Phys. Fluids **27**, 085101 (2015).

[62] J. Jeong and F. Hussain, On the identification of a vortex, J. Fluid Mech. **285**, 69 (1995).

[63] Y. S. Baik, L. P. Bernal, K. Granlund, and M. V. Ol, Unsteady force generation and vortex dynamics of pitching and plunging aerofoils, J. Fluid Mech. **709**, 37 (2012).

[64] L. Graftieaux, M. Michard, and N. Grosjean, Combining PIV, POD and vortex identification algorithms for the study of unsteady turbulent swirling flows, Meas. Sci. Technol. **12**, 1422 (2001).